ADVANCED OPTICAL MATERIALS

Supporting Information

for *Adv. Optical Mater.*, DOI: 10.1002/adom.201600448

Enhancing the Angular Sensitivity of Plasmonic Sensors Using Hyperbolic Metamaterials

Kandammathe Valiyaveedu Sreekanth, Yunus Alapan, Mohamed ElKabbash, Amy M. Wen, Efe Ilker, Michael Hinczewski, Umut A. Gurkan, Nicole F. Steinmetz, and Giuseppe Strangi**

Supporting Information: Enhancing the angular sensitivity of plasmonic sensors using hyperbolic metamaterials

Kandammathe Valiyaveedu Sreekanth, Yunus Alapan, Mohamed ElKabbash, Amy M. Wen, Efe Ilker, Michael Hinczewski, Umut A. Gurkan, Nicole F. Steinmetz and Giuseppe Strangi

Materials and Methods

GC-HMM fabrication: HMMs were produced by the sequential deposition of Al_2O_3 and Au layers on a glass substrate (Micro slides, Corning) using electron beam evaporation of Al_2O_3 pellets and thermal evaporation of Au pellets (both from Kurt J. Lesker Co.). The deposition rates of dielectrics and metals were set to be 0.5 A/s and 0.3 A/s, respectively. 2D metal (Au) diffraction gratings were realized on top of the HMM by electron beam lithography (Tescan Vega). Initially, a methyl methacryllate (MMA) resist (8.5MMAEL 11, MICROCHEM) was spin coated on the sample at 4000 rpm and baked at 180ºC for 5 min. A PMMA resist (950PMMA C2 Resist, MICROCHEM) was later spin coated at 5000 rpm and baked at 180ºC for 8 min. The prepared samples were patterned by E-beam lithography at a dosage of 150 mC/cm^2. The exposed samples were developed using a methyl isobutyl ketone (MIBK) and isopropyl alcohol (IPA) solution for 90 s, and IPA for 30 s. A 20 nm thick Au thin film was then deposited directly on top of the sample by the thermal evaporation of Au pellets as above.

Microfluidic channel integration with the GC-HMM: PMMA caps were prepared by laser micromachining an inlet and outlet (diameter 0.61 mm, separation 12.4 mm) using a VersaLASER system (Universal Laser Systems Inc., Scottsdale, AZ). Double-sided adhesive film (iTapestore, Scotch Plains, NJ) was machined to encompass the PMMA component and 14 x 2 mm microchannels 50 µm in height. The film was attached to the PMMA component to include the inlet and outlet between the outline of the channels. The GC-HMM substrate was

then assembled with the PMMA–film structure to form microfluidic channels within the sensing device.

Optical characterizations: Variable angle spectroscopic ellipsometry (J. A. Woollam Co., Inc, V-VASE) was used to determine the thicknesses and optical constants of the Au and Al_2O_3 thin films. The reflection spectra as a function of excitation wavelength and incident angle were acquired using the same instrument. The spectroscopic and angular resolution of the instrument are 0.03 nm and 0.01 degrees, respectively. In the biosensing experiments, the angular resolution was set to 0.1 degrees. A scanning time of around 60 seconds is required to record around 140 data points for each measurement. Hence, the time required for recording one data point is around 0.4 seconds, which is higher than the minimum measurement time of the instrument (0.1 seconds). Therefore, the noise level is well below the signal amplitude.

Biosample preparation: Glycerol solutions with weight percentage concentrations of 0.1–1% (w/v) were prepared in distilled water. Biotin solutions with varying concentrations (100 pM to 10 μM) were prepared by serial dilution in distilled water (1:10). N-γ-maleimidobutyryl-oxysulfosuccinimide ester (GMBS) stock solution was prepared by dissolving 25 mg GMBS in 0.25 mL DMSO, and the stock solution was diluted in ethanol to obtain a 0.28% (w/v) GMBS working solution. A 4% (w/v) solution of 3-maleimidopropionate (3-MPS) was prepared in ethanol. Neutravidin (1 mg/mL) was prepared by dissolving 10 mg of the protein in 1 mL distilled water and then diluting in PBS (1:10).

Surface chemistry: The GC-HMM substrates were cleaned using a UV ozone cleaner (Novascan PSDP-UV8T) for 5 min at 60°C, immediately dipped in ethanol, and then immersed in 3-MPS solution for 30 min at room temperature. The GC-HMM substrates were then dipped in ethanol and immersed in GMBS solution for 15 min at room temperature. The substrates were

then dipped in ethanol and distilled water before drying under nitrogen. The microfluidic channels were then joined to inlet and outlet tubes and the channels were flushed with PBS. Neutravidin solution was then injected into the microchannels and incubated for 45 min at room temperature before flushing again with PBS again to remove excess neutravidin.

CPMV preparation: CPMV was propagated in *Vigna unguiculata* (black-eyed pea) plants 10-14 days after planting using mechanical inoculation with a 0.1 mg/mL solution of CPMV. Viral particles were isolated using a combination of blending, chloroform/butanol extraction, and centrifugation based on established methods. CPMV concentrations were determined by UV/visible spectroscopy, with a molar absorptivity coefficient for CPMV of 8.1 mg^{-1} mL cm^{-1} at 260 nm. To confirm structural integrity, particles were diluted in distilled water and adsorbed onto formvar carbon-coated copper grids at a concentration of 0.1 mg/mL for 5 minutes. This was followed by a brief wash with distilled water then negative staining with 2% (w/v) uranyl acetate for 2 minutes. Imaging was performed using a Zeiss Libra 200FE transmission electron microscope at 200 kV. Imaging confirmed the presence of intact 30 nm-sized CPMV particles; aggregates or broken particles were not detectable.

Effective medium approximations: The uniaxial permittivity components of fabricated HMM derived using effective medium theory (EMT) is shown in **Figure S1**. Experimentally obtained dielectric constants of gold and aluminum dioxide were used in the calculation. Blue and black lines represent the real and imaginary parts of ε_{ll} , and pink and red lines represent the real and imaginary parts of $\varepsilon_{\perp}$, respectively.

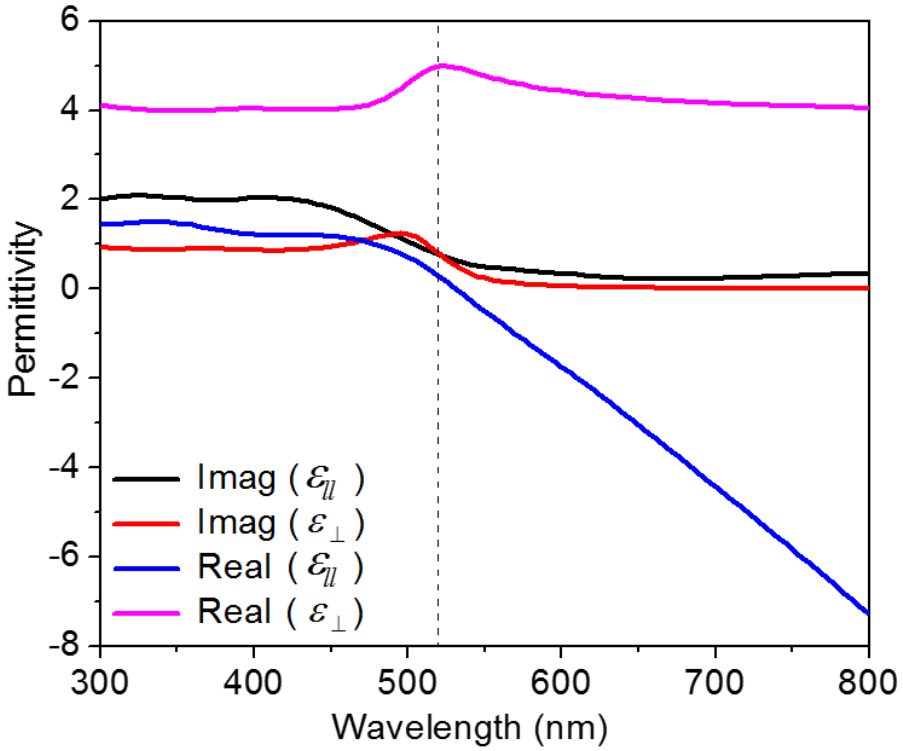

Figure S1. EMT-derived real and imaginary parts of the effective uniaxial permittivity components of the Au-Al_2O_3 HMM.

Modal index of SPP and BPP modes: The modal index of SPP and BPP modes [1] are given by,

$$n_{SPP} = \sqrt{\frac{\varepsilon_m \varepsilon_d}{\varepsilon_m + \varepsilon_d}} \quad \text{for SPP} \qquad (1)$$

$$n_{BPP_0} = \sqrt{\frac{\varepsilon_d \varepsilon_m (t_d + t_m)}{t_d \varepsilon_m + t_m \varepsilon_d}} \quad \text{for BPP} \qquad (2)$$

Where (ε_d, t_d) and (ε_m, t_m) are the dielectric constant and thickness of dielectric and metal, respectively. We then calculated the modal index of SPP and fundamental BPP modes as a function of wavelength. As shown in **Figure S2**, the modal index of both modes decreases with increasing wavelength. In the simulation, the optical constants of gold are calculated based on

Drude free-electron theory, $\varepsilon_m = 1 - \left(\frac{\omega_p^2}{\omega(\omega + i/\tau)} \right)$ where ω_p is the plasma frequency of gold and τ is the relaxation time.

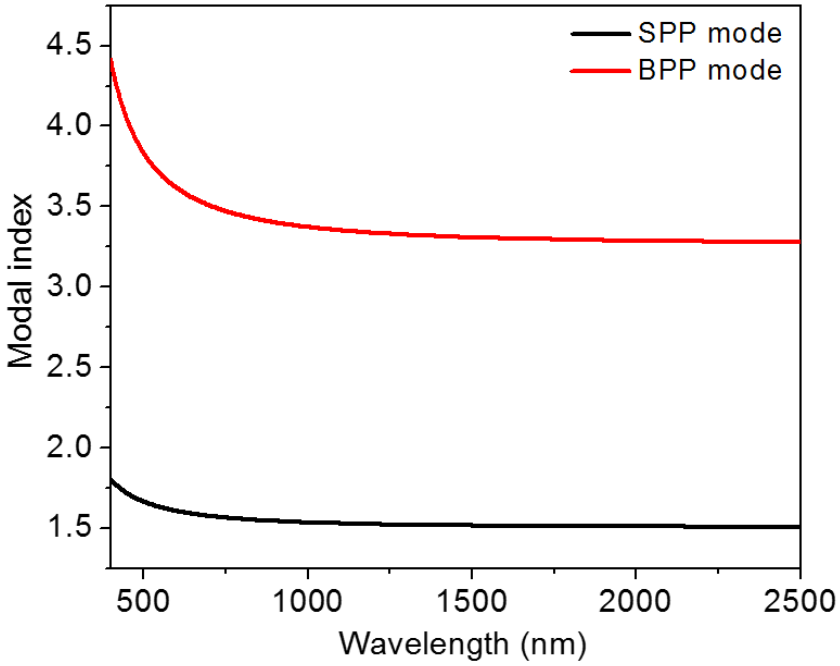

Figure S2. Variation of modal index of SPP and BPP modes with wavelength

Modal dispersion: Since no exact formal theory is available for the grating-induced coupling for the BPP excitation, here we provide an alternative approach based on the method described in Ref [2], to study the dispersion of surface and BPP modes.

In this analysis, we assume that HMM is a subwavelength one-dimensional photonic crystal, to relate the BPP mode excitation with the dispersion of the multilayer stack. **Figure S3** shows the dispersion diagram (band structure) of frequency versus wave vector projected in to the plane of the interface of the structure for TM polarized waves. Such diagram is usually plot to relate the experimental surface wave dispersion results to photonic band gap of the periodic stack [2-4].

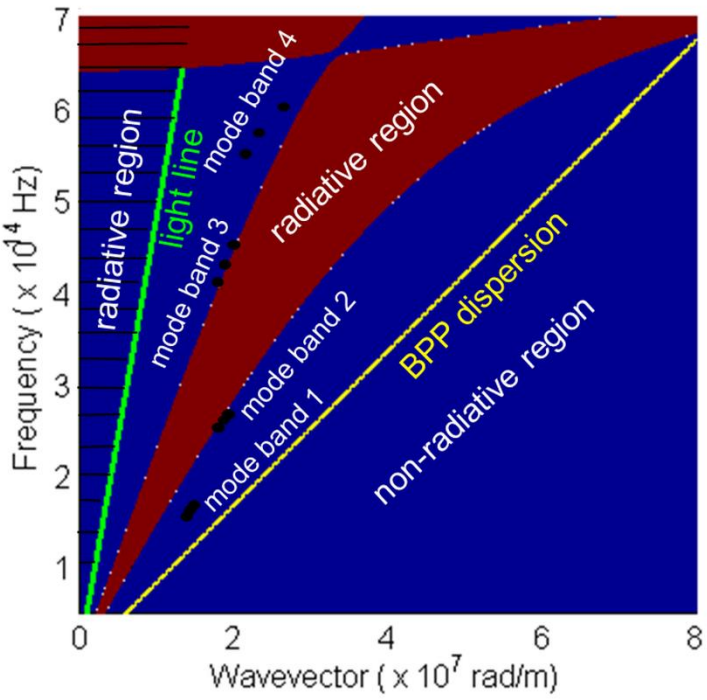

Figure S3 Surface dispersion diagram (band structure) of Au-Al_2O_3 multilayer stack for TM polarization.

In **Figure S3**, blue and red dark regions represent the non-radiative and radiative regions within the HMM, respectively. At any given frequency, incident light can have wave vector values ranging from zero (normal incidence) to a maximum value of 2πf/c (light travelling tangentially parallel to the surface, i.e. $\theta=90^{o}$). Therefore, we plotted the light line for air using the maximum value (2πf/c) and indicated by green solid line in the dispersion diagram. The area limited by this line (hatched region) corresponds to surface wave vector values that are radiative on the air side of the interface. The SPP and BPP modes exist in the non-radiative regions of the dispersion diagram and away from the air light line.

We then calculated the parallel wave vector of the surface modes at all BPP mode bands (2100 nm to 2050 nm, 1100 nm to 1050 nm, 750 nm to 700 nm, and 550 nm to 500 nm.) using the expression, $kx=k_0 sin\theta \pm mk_g$, where $k_0=2\pi/\lambda$, $kg=2\pi/\Lambda$ with Λ being the period of the grating, θ

being the resonance angle and *m* being the diffraction orders. Here we assumed m=+1. The experimentally obtained wave vector values are indicated by black dot in the dispersion diagram. It is visible from the figure that these values appear away from the air light line and occur close to band edge, but within the non-radiative region of the dispersion diagram.

BPP modal dispersion is then obtained using the expression [1], $k_{BPP} = k_0\sqrt{\varepsilon_d - \frac{\lambda^2}{\pi^2 t_d t_m}\frac{\varepsilon_d}{\varepsilon_m}}$ with (t_d, ε_d) and (t_m, ε_m) are the thickness and dielectric permittivity of Al_2O_3 and gold, respectively. The yellow solid line in the dispersion diagram represents the BPP modal dispersion, which is in the non-radiative region and well beyond the parallel wave vector of the surface modes at all frequencies. As expected, the surface modes exist between the air light line and BPP modal dispersion and within the non-radiative region. Even though this plot does not provide the direct evidence of the grating-induced coupling of the SPP and BPP modes, it can provide information about the modal dispersion of surface and bulk plasmon modes. Since the modal index of BPP modes are higher than that of the surface modes, the grating diffraction orders also play an important role in the grating-induced coupling of SPP and BPP modes. A detailed theoretical analysis about the role of the grating diffraction orders on the selection mechanisms of the BPP modes will be published elsewhere.

Reflectance spectrum of sensor device: Reflectance spectra of the sensor device under a DI water environment is shown in **Figure S4**. In contrast to the reflectance spectrum of GC-HMM (without channel), the fourth BPP mode at 2000 nm is missing due to the greater absorption capacity of the relatively thick PMMA channel at longer wavelengths. A blue shift in resonance wavelength with respect to incident angle proves that all the modes are guided modes. The blue shift is due to the fact that the resonance angle increases in each BPP wavelength band when the

excitation wavelength decreases. That means a higher resonance angle is required for the excitation of BPP modes at shorter wavelengths for each BPP band.

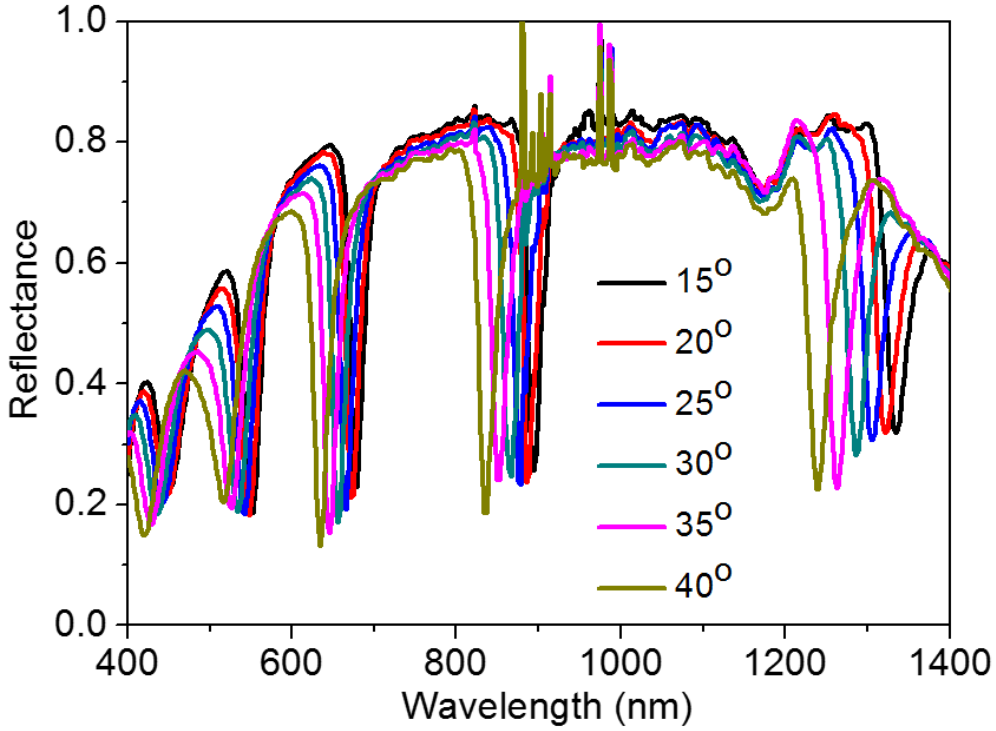

Figure S4. Reflectance spectra of the sensor device at different angles of incidence when DI water was used as the superstrate.

Sensor evaluation using glycerol solution: Reflectance spectra as a function of incident angle of the sensor device under DI water and 0.1% (w/v) glycerol in DI water are shown in **Figure** S5. Different angular shifts were obtained at different excitation wavelengths. The maximum shift (0.7 degrees) was obtained at 1250 nm and the minimum shift (0.2 degrees) at 530 nm.

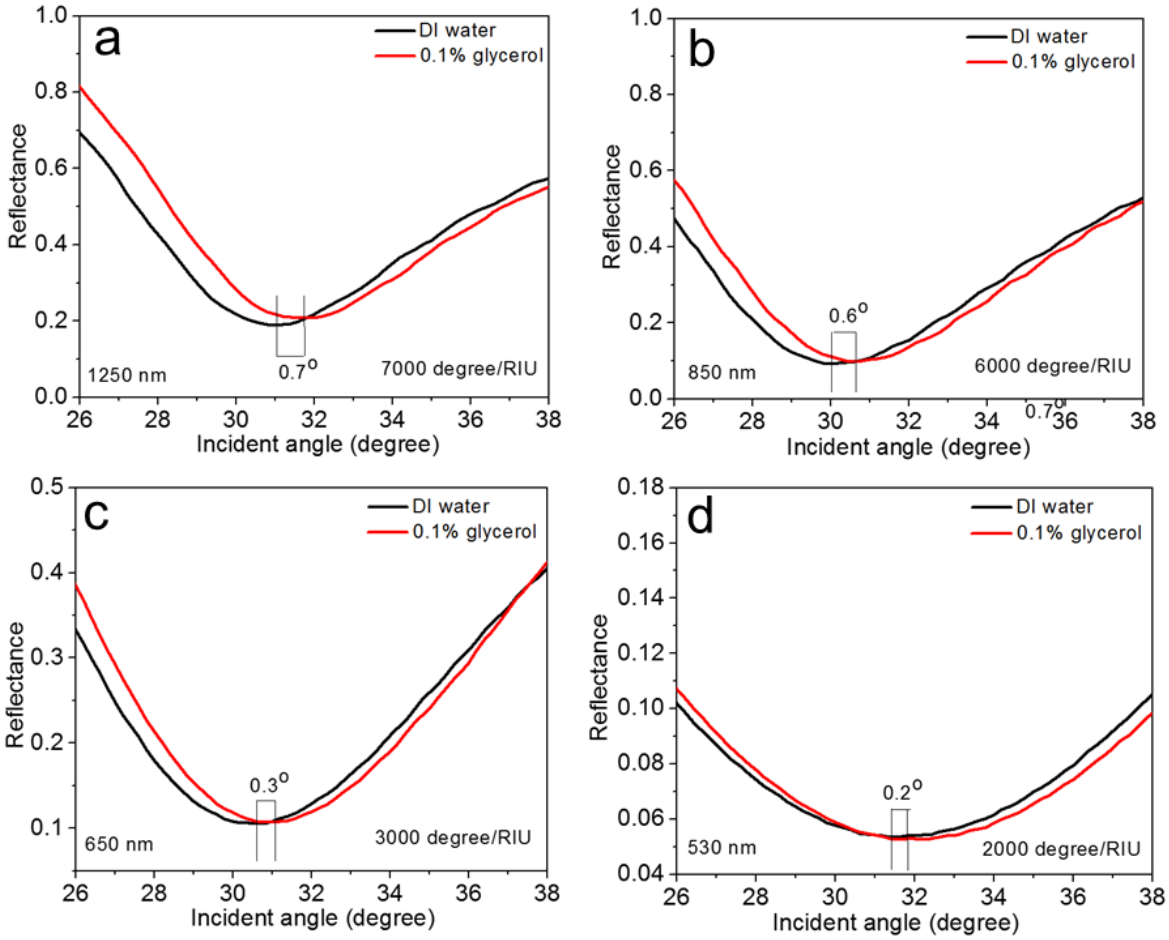

Figure S5. Reflectance spectrum when DI water and 0.1 % glycerol in DI water were used as the superstrate at (a) 1250 nm, (b) 850 nm, (c) 650 nm, and (d) 530 nm.

Binding of CPMV on the sensor surface: The binding of CPMV to the sensor surface was investigated by recording the reflectance spectrum over time. The reflectance spectra of the sensor obtained by injecting 100 fM CPMV in PBS with time progress is shown in **Figure S6**. An increase in angular shift with time was obtained, which is due to statistical fluctuations where larger or smaller number of binding events occur. In this study, the angular resolution of the instrument was set to be 0.5 degrees and the spectrum was recorded every 60 seconds. For simplicity, only limited spectra are shown in **Figure S6**. It is evident that the angular shift almost

saturated at 15-20 min. No considerable shift was noticed after 20 min. A maximum angular shift of 3 degrees was obtained for 100 fM CPMV after 20 min.

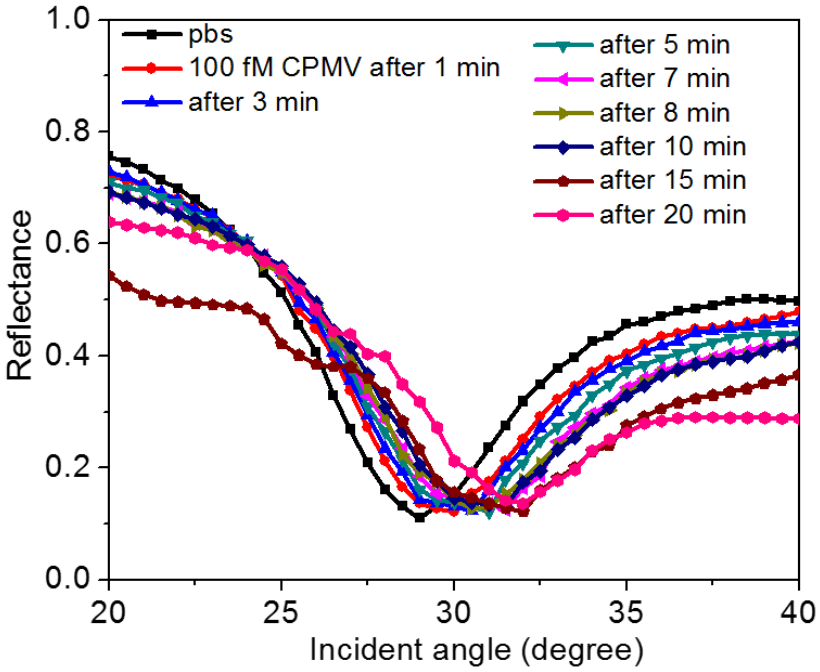

Figure S6. Reflectance spectrum of 100 fM CPMV in PBS over time.

Sensitivity of the angular shift to the number of adsorbed molecules: In this section we analyze the sensitivity of the angular shift to the number of adsorbed molecules on the sensor surface. We consider the saturation values of the angular shift $\Delta\theta$ (which occurs approximately after 45 mins) for different concentrations c of biotin in PBS (with a functionalized surface) and of CPMV in PBS. The shift of the resonance angle depends on the number of bound molecules $N(c)$ in the sensing region. Though we cannot directly measure the precise value of $N(c)$, we can reliably estimate an upper bound $N_{\max}(c)$ based on the sensor parameters, such that the actual $N(c) \le N_{\max}(c)$ at any concentration (see supporting information in Ref. [5] for a detailed analysis). The end result is that $N_{\max}(c) = 8.4\, c \times 10^{15}$ M^{-1}.

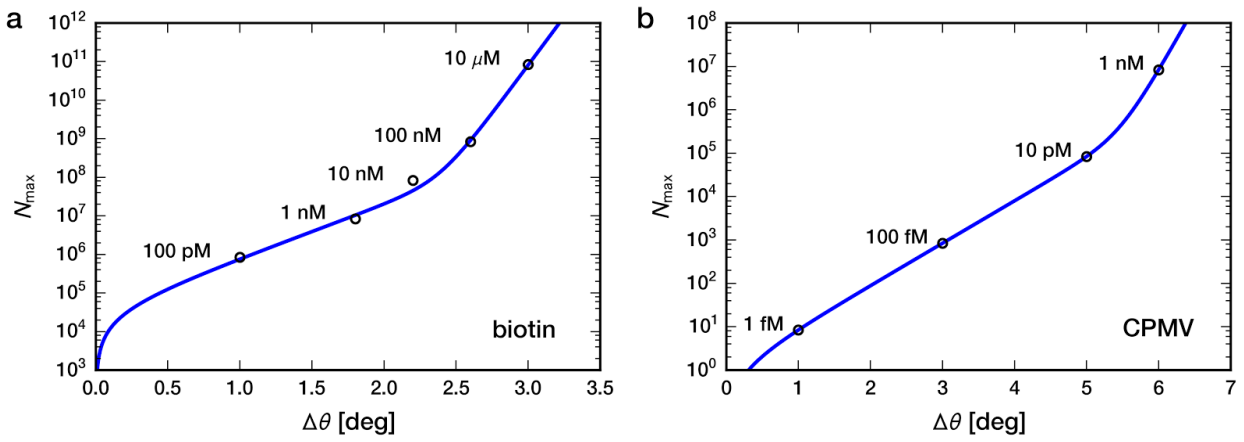

Figure S7: Experimental results (circles) for the maximum possible number of adsorbed particles in the sensor region, $N_{\max}(c)$, versus angular shift $\Delta\theta(c)$, at various concentrations c indicated in the labels. The blue curves are best-fit results to the phenomenological model in Eq. (3). Panel a corresponds to biotin in PBS with a functionalized surface, and panel b corresponds to CPMV in PBS. The best-fit parameters for the two cases are: a) A_1=3.1 × 10^4, A_2=6.1 × 10^{-5}, β_1=0.31°, β_2=0.086°; b) A_1=0.99, A_2=1.6 × 10^{-11}, β_1=0.44°, β_2=0.15°.

We observed in Ref. [5] that there was a nonlinear relationship between $N_{\max}(c)$ and $\Delta\lambda(c)$, the shift in resonance wavelength at concentration c. This behavior could be accurately represented using a phenomenological double-exponential fitting function, and we find an analogous functional relationship between $N_{\max}(c)$ and $\Delta\theta(c)$. It takes the form:

$$N_{\max} = A_1(e^{\Delta\theta/\beta_1} - 1) + A_2(e^{\Delta\theta/\beta_2} - 1) \qquad (3)$$

Where A_1, A_2, β_1, β_2, are fitting parameters. The function is chosen such that the limiting behavior at small $\Delta\theta$ is linear, as we would expect in the case of very few adsorbed particles. **Figure S7** shows the experimental N_{max} versus $\Delta\theta$ results for biotin and CPMV as circles, with the best-fits of Equation (3) drawn as solid curves. In the case of CPMV, at the

smallest probed concentration (1 fM) the value for N_{max} is approximately 8 adsorbed particles, indicating that we are close to the single-particle detection regime.

References

[1] I. Avrutsky, I. Salakhutdinov, J. Elser, V. Podolskiy, *Phys. Rev. B* **2007**, 75, 241402.

[2] P. Yeh, A. Yariv, C. -S. Hong, *J. Opt. Soc. Am.* **1977**, 67, 423.

[3] W. M. Robertson, M. S. May, *Appl. Phys. Lett.* **1999**, 74, 1800.

[4] J. A. Gaspar-Armenta, F. Villa, T. Lopez-Rios, Opt. Comm. **2003**, 216, 379.

[5] K. V. Sreekanth, Y. Alapan, M. ElKabbash, E. Ilker, M. Hinczewski, U. A. Gurkan, A. De Luca, G. Strangi, *Nat. Mater.* **2016,** 15, 621.